Marine Heatwaves across the central South Pacific: characteristics, mechanisms, and modulation by the El Niño Southern Oscillation

Bastien Pagli[1], Takeshi Izumo[1], Alexandre Barboni[2], Carla Chevillard[3], Cyril Dutheil[4], Raphaël Legrand[5], Christophe Menkes[6], Claire Rocuet[1] and Sophie Cravatte[7]

[1]*UMR 241 SECOPOL, (IRD, ILM, Ifremer, UPF), Tahiti, French Polynesia*

[2]*Laboratoire d'Etudes en Géophysique et Océanographie Spatiales (LEGOS), Toulouse, France*

[3]*IFREMER, Tahiti, French Polynesia*

[4]*MARBEC, University of Montpellier, CNRS, Ifremer, IRD, Sète, France*

[5]*DIRPF, Météo France, Tahiti, French Polynesia*

[6]*ENTROPIE (IRD, Ifremer, Université de la Réunion, Université de la Nouvelle-Calédonie), Nouméa, New Caledonia*

[7]*Université de Toulouse, LEGOS (IRD, CNES, CNRS, UT3), Toulouse, France.*

Correspondence to: Bastien Pagli (bastien.pagli@ird.fr)

Supplementary Information

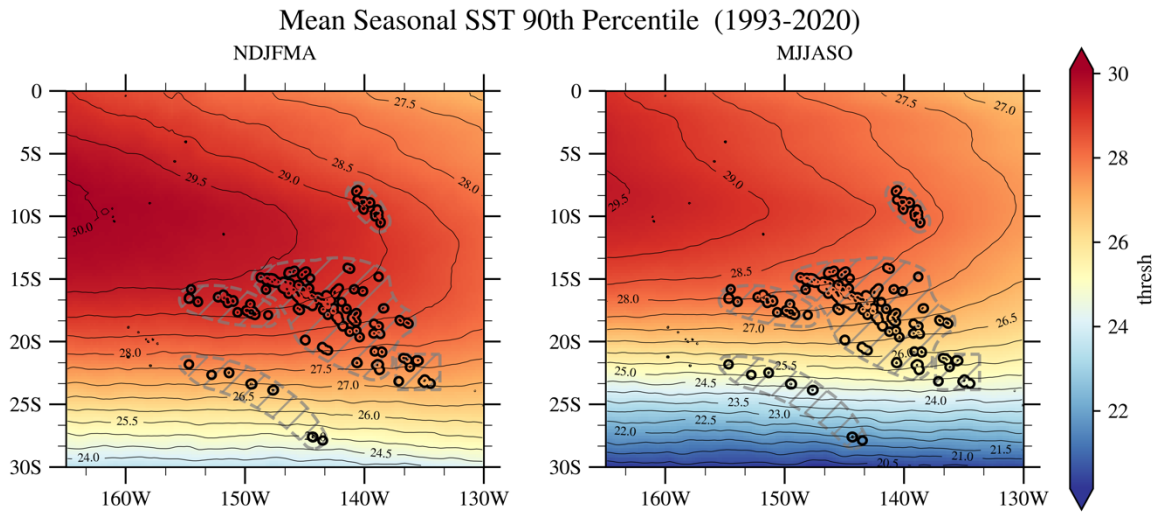

Figure S1. Seasonal average of the 90th percentile of sea surface temperature (SST) over FP during (left) NDJFMA and (right) MJJASO. Black contours indicate isotherms at 0.5 °C intervals.

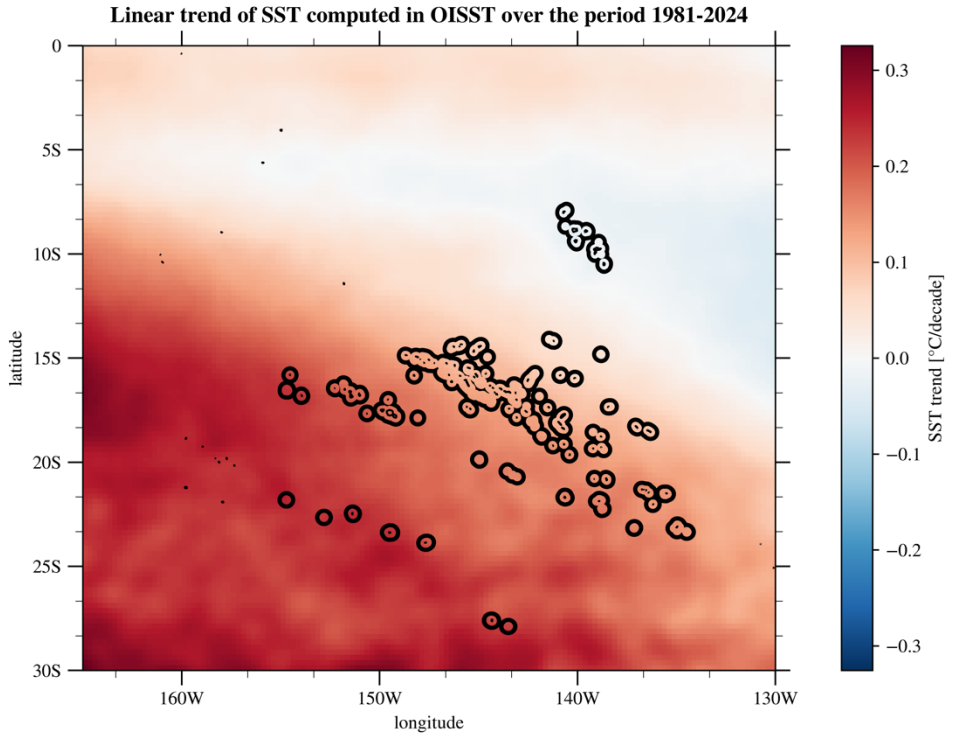

Figure S2. Linear trend computed in OISST over 1981-2024 expressed in °C per decade.

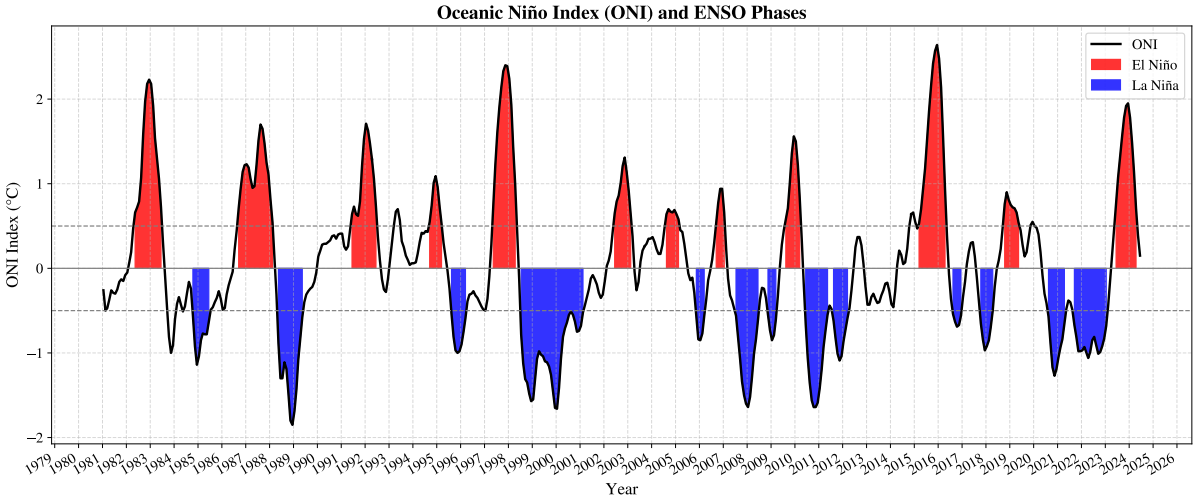

Figure S3. ONI index over 1981-2024 from NOAA. El Niño (La Niña) periods - defined following the NOAA criteria (cf. Methods in section 2.2 of the manuscript) - are highlighted in red (blue).

Table 1. ENSO classification of the austral summer seasons (November to April) as performed in (Pagli et al., 2025a,b). The number of years (*n*) is indicated in the left column.

ENSO clusters	**Years**
Extreme EPEN (Eastern Pacific El Niño) n=2	82/83, 97/98
Strong MEN (Mixed El Niño) n=3	91/92, 15/16, 23/24
CPEN (Central Pacific El Niño) n=7	83/84, 86/87, 87/88, 92/93, 94/95, 02/03, 09/10
EPLN+N (Eastern Pacific La Niña + Neutral years) n=21	81/82, 84/85, 85/86, 89/90, 90/91, 93/94, 95/96, 96/97, 01/02, 03/04, 04/05, 06/07, 11/12, 12/13, 13/14, 14/15, 16/17, 17/18, 18/19, 19/20, 22/23
CPLN (Central Pacific La Niña) n=8	88/89, 98/99, 99/00, 00/01, 05/06, 07/08, 08/09, 20/21
Strong MLN (Mixed La Niña) n=2	10/11, 21/22

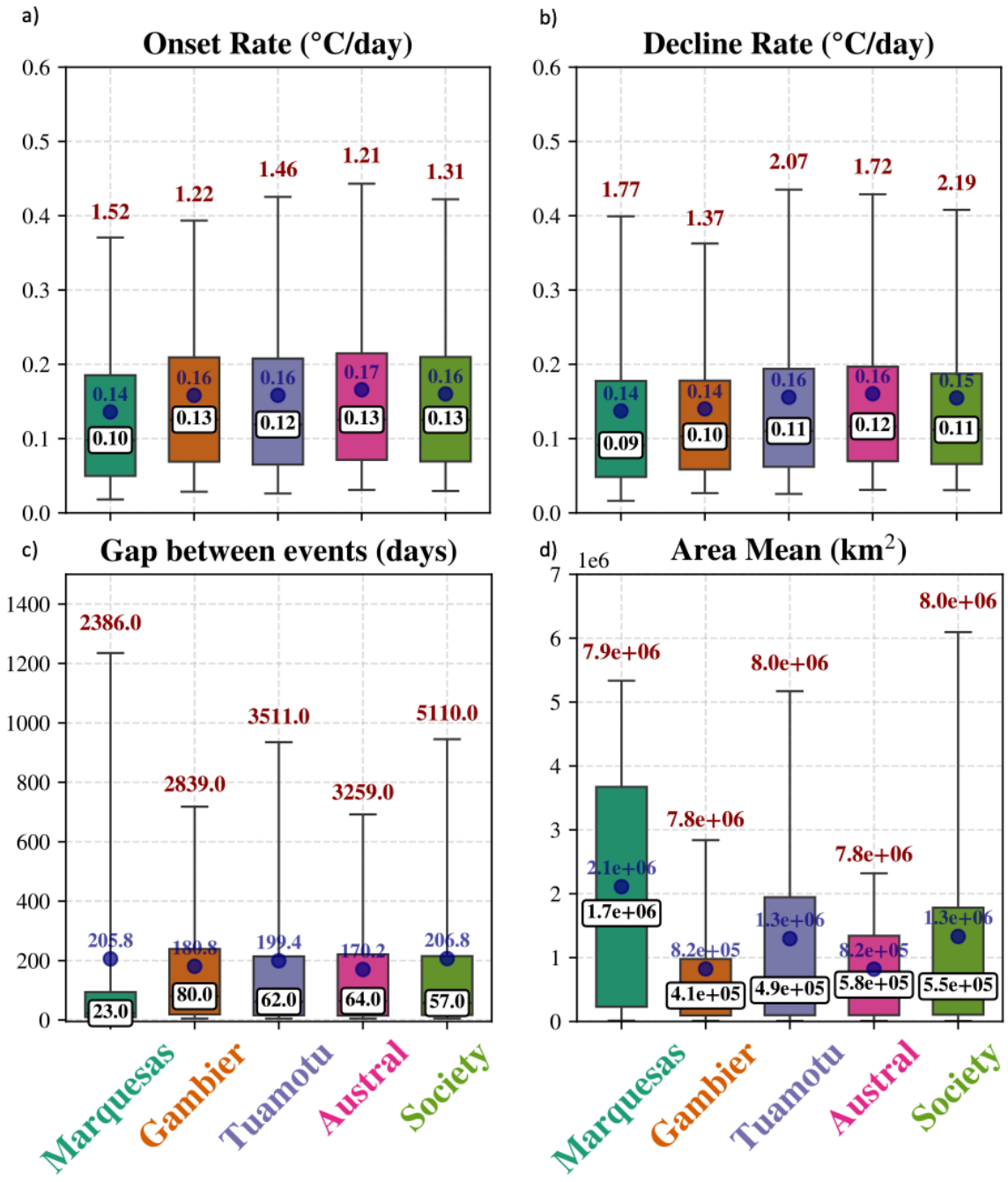

Figure S4. Additional MHW metrics' distributions, averaged for each archipelago, shown here without distinguishing between warm and cold seasons. Panels a and b present the distributions of onset and decline rates, respectively, calculated across all MHW events for each archipelago. Panel c illustrates the distribution of the number of days between consecutive MHWs and panel d shows the distribution of the mean area (across the event's duration) associated to each MHW detected locally. The box plots follow the same conventions as those used in Fig. 2 of the main manuscript.

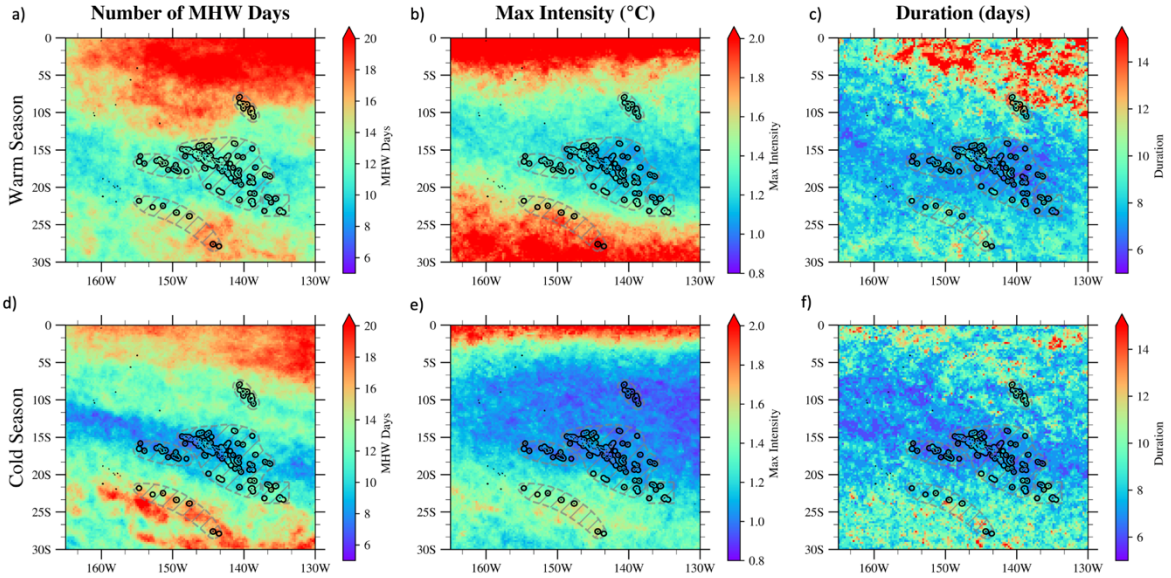

Figure S5. As in Fig. 1 but for MHWs detected on the detrended SST dataset (OISST).

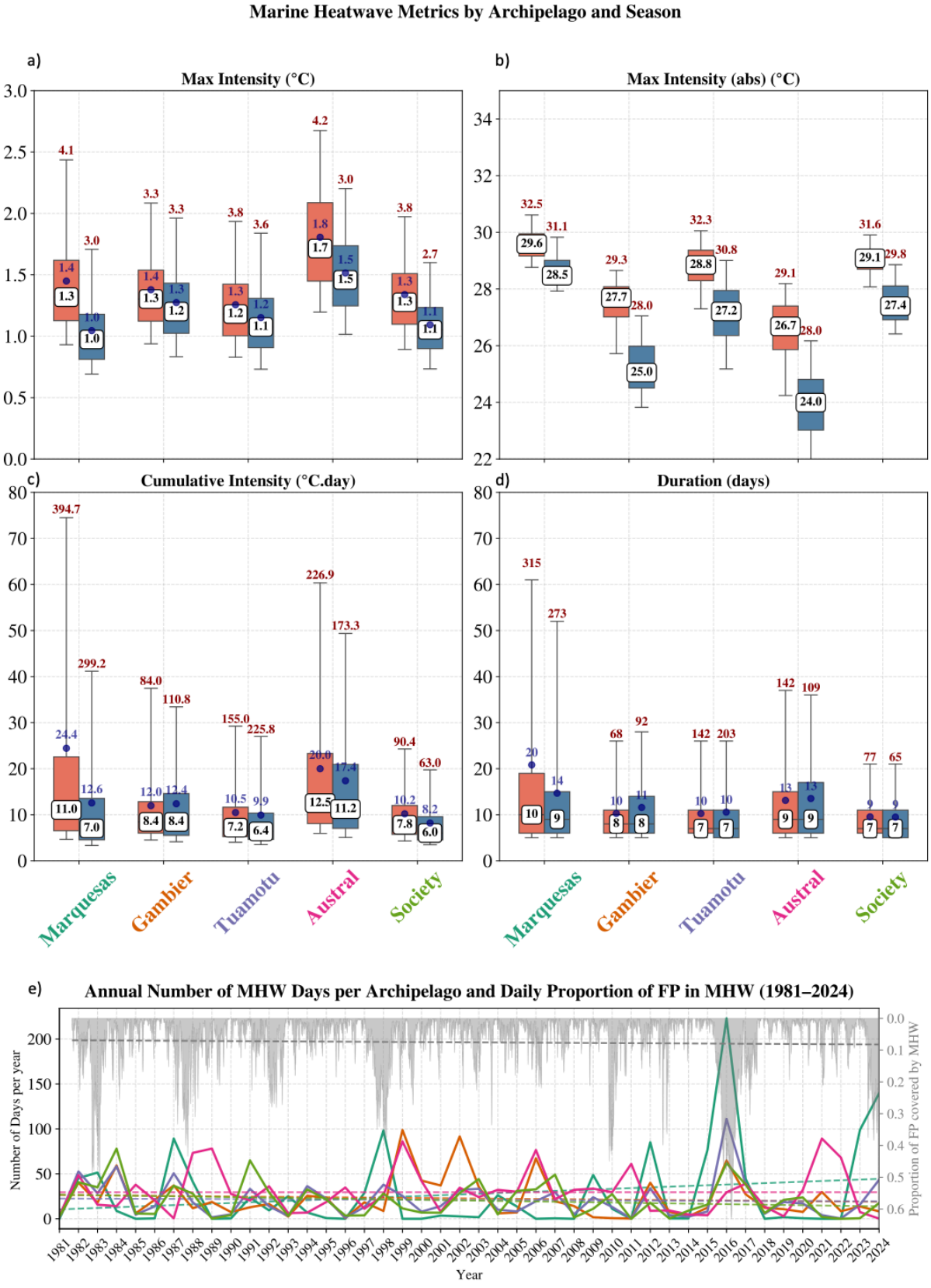

Figure S6. Same as Fig. 2 but for MHWs detected on the detrended SST dataset (OISST).

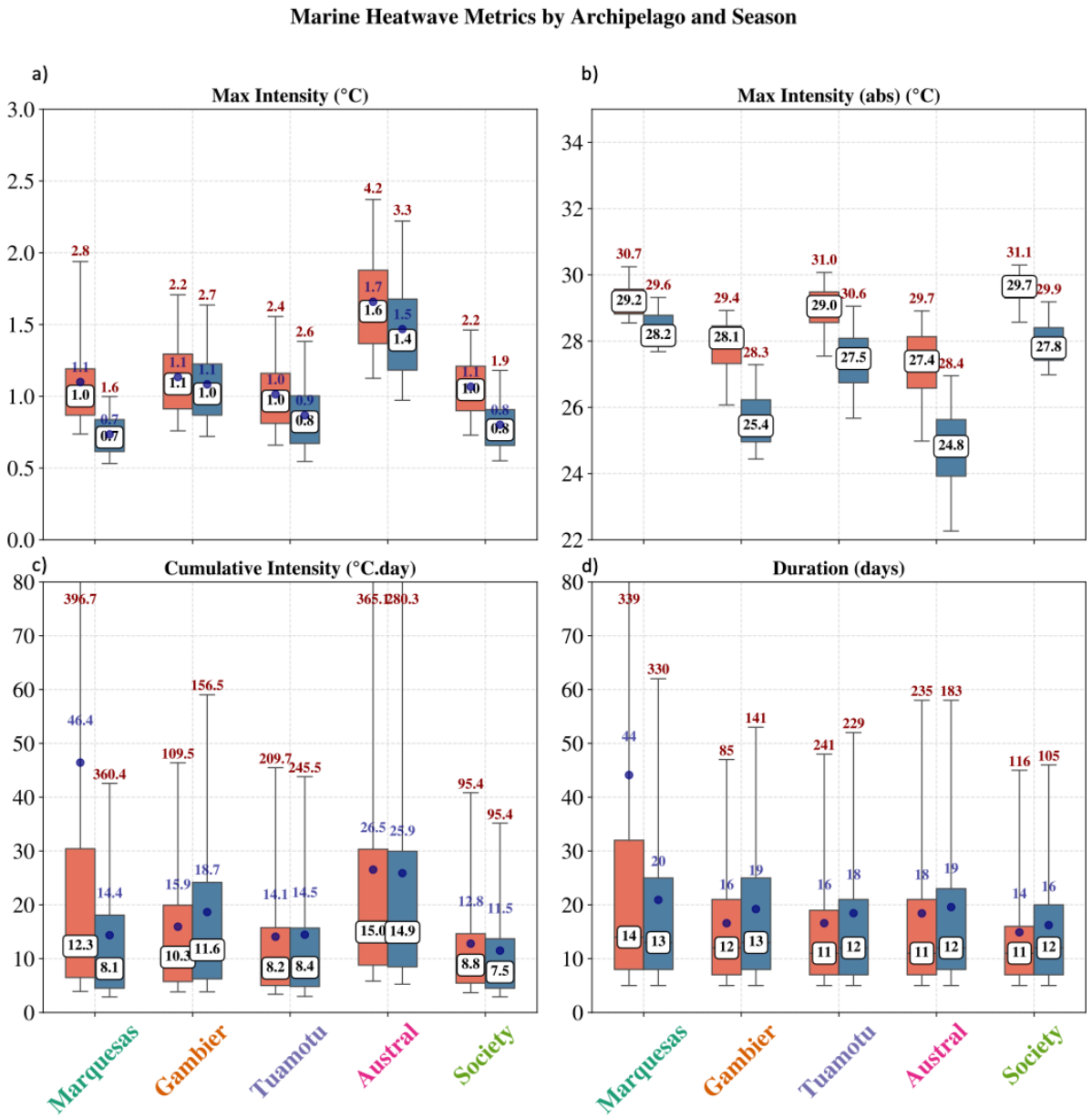

Figure S7. Same as Fig. 2 but for MHWs detected in GLORYS over 1993-2024. No detrending has been performed on SST data prior to MHW detection. For Q95 values that exceed the y-axis limit in Fig. 2, the maximum value is indicated at the top of the corresponding bar.

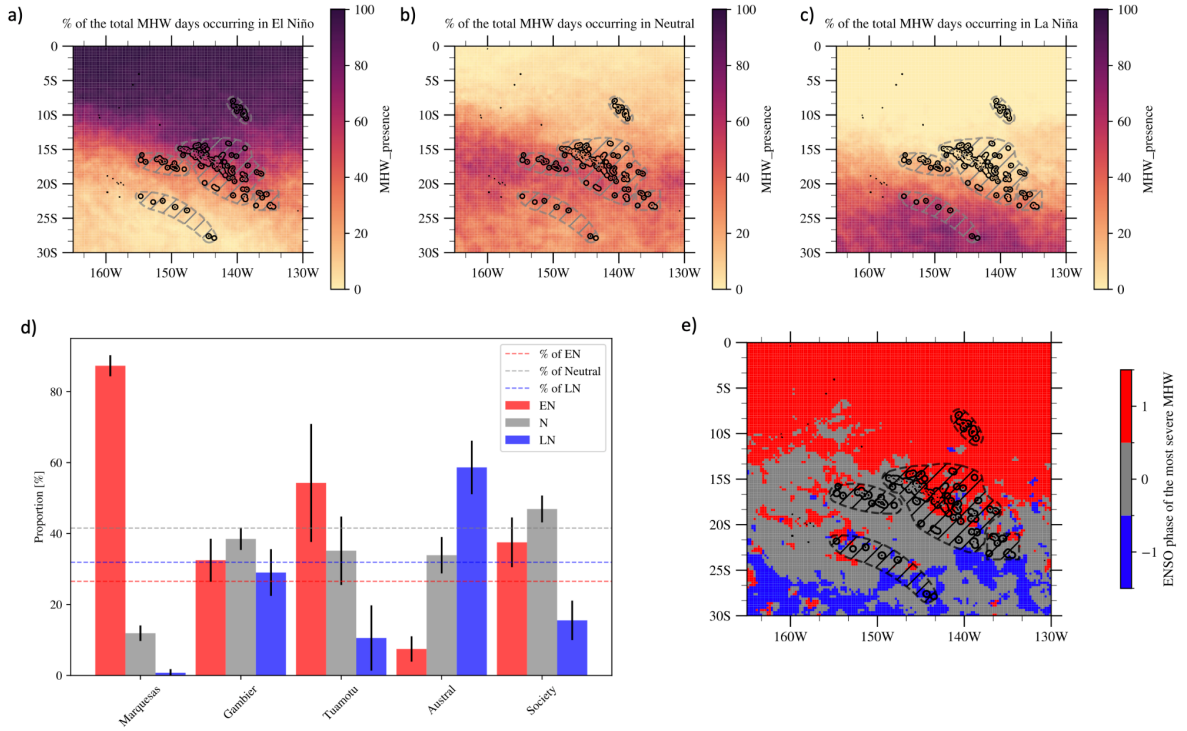

Figure S8. As Fig. 3 but considering only summer months (NDJFMA).

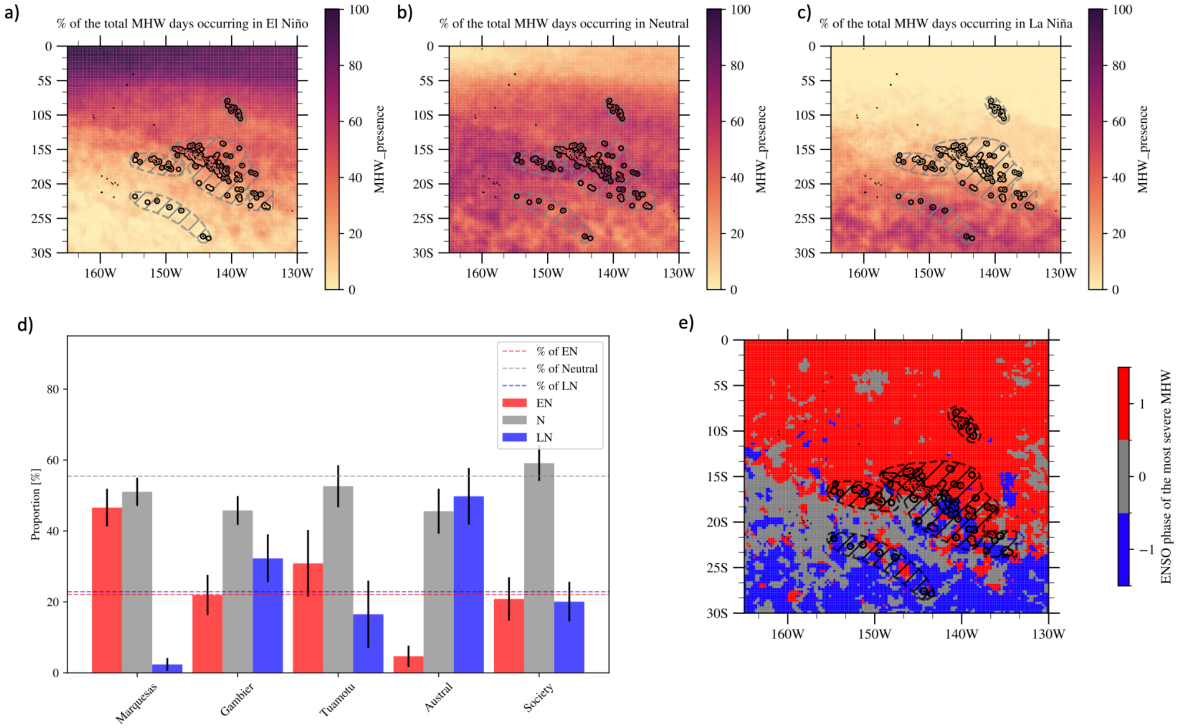

Figure S9. As Fig. 3 but considering only winter months (MJJASO).

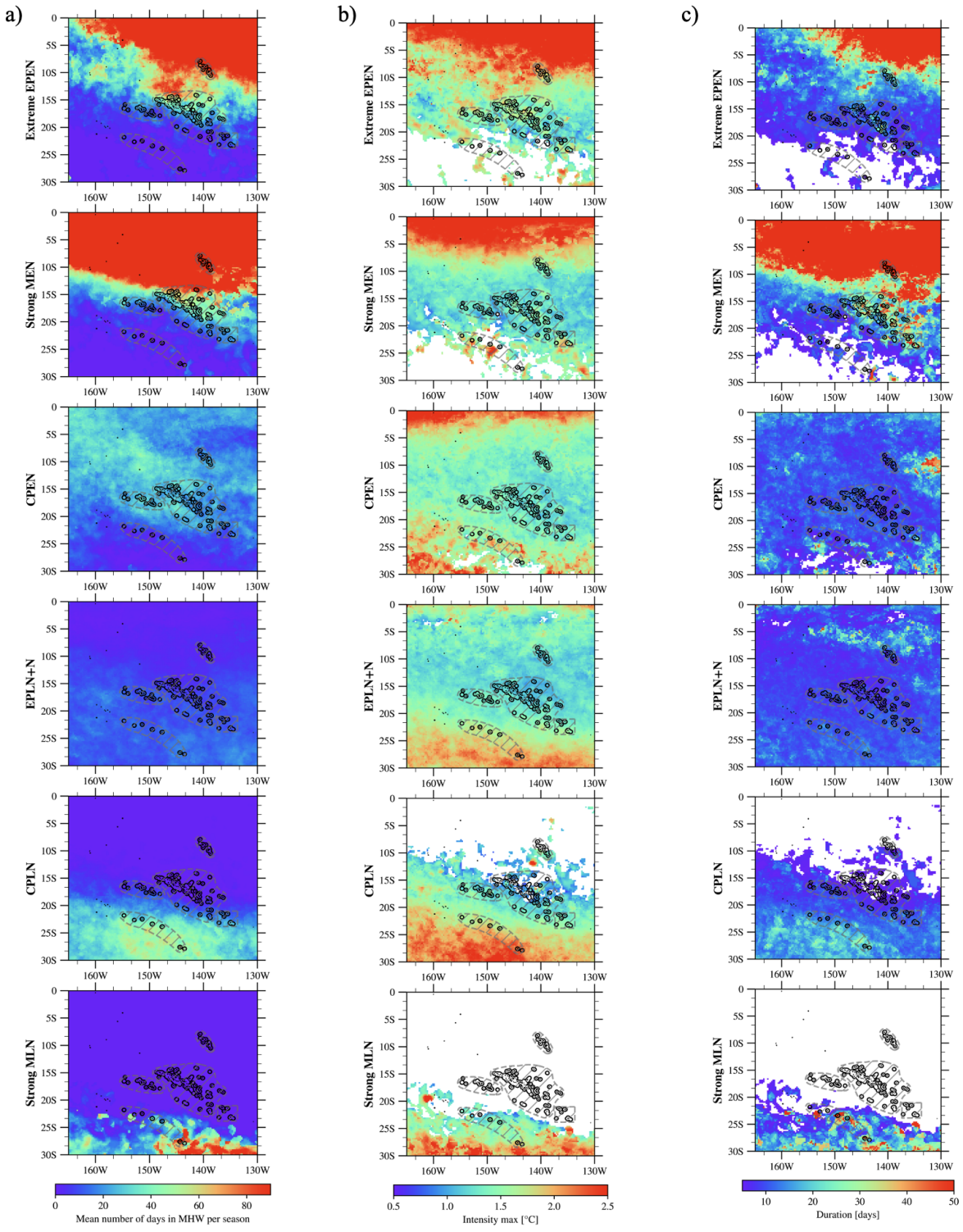

Figure S10. ENSO clusters composites (average across years of each cluster) of the number of MHW days (a) per austral summer season (NDJFMA), along with the maximum intensity (b) reached during events and their duration (c).

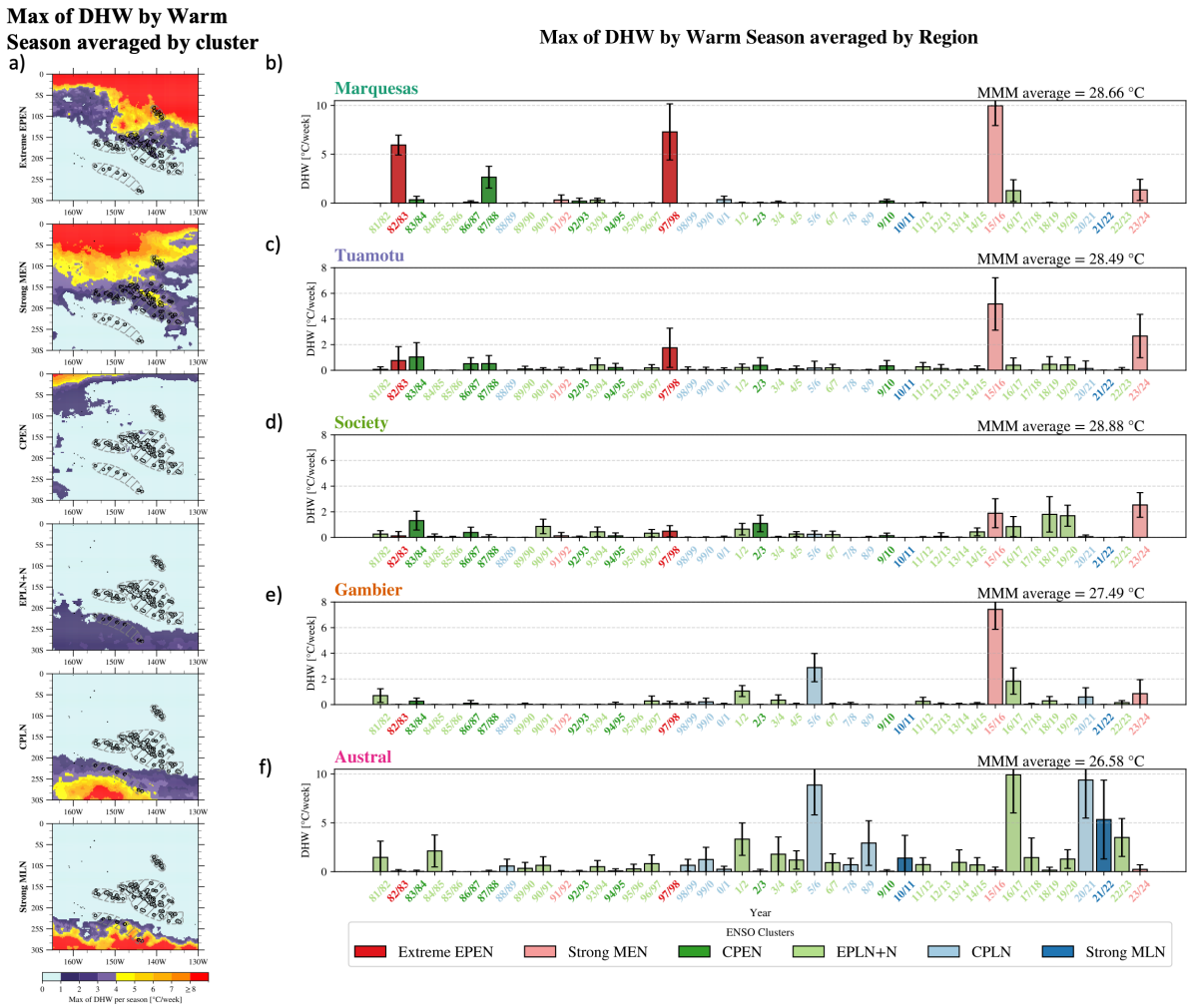

Figure S11. Same as Fig. 5 but without having removed the trend before the DHW calculation detection.

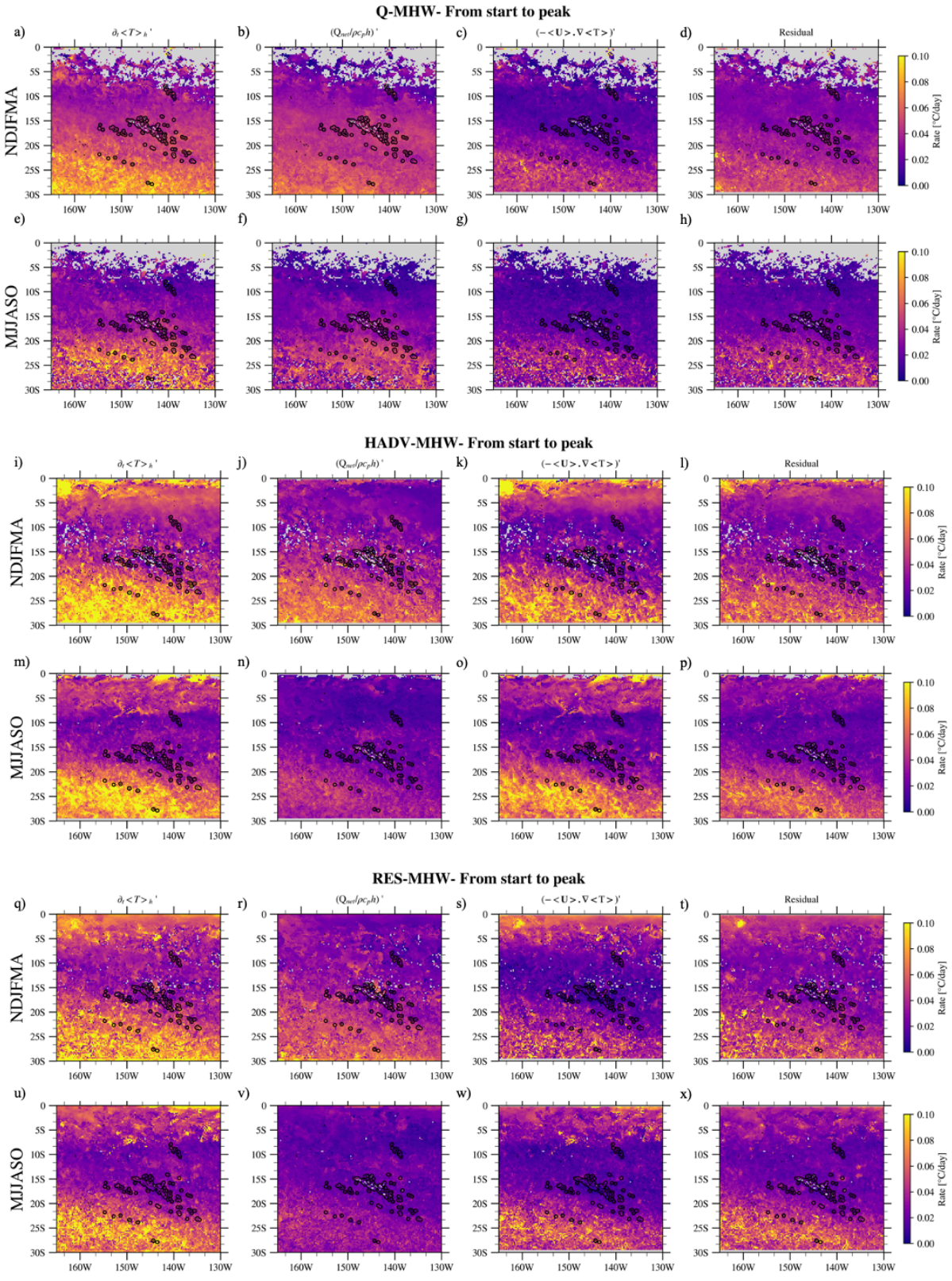

Figure S12. Standard deviation associated to the mean composites of the heat budget terms of Eq. (2) presented in Fig. A1.

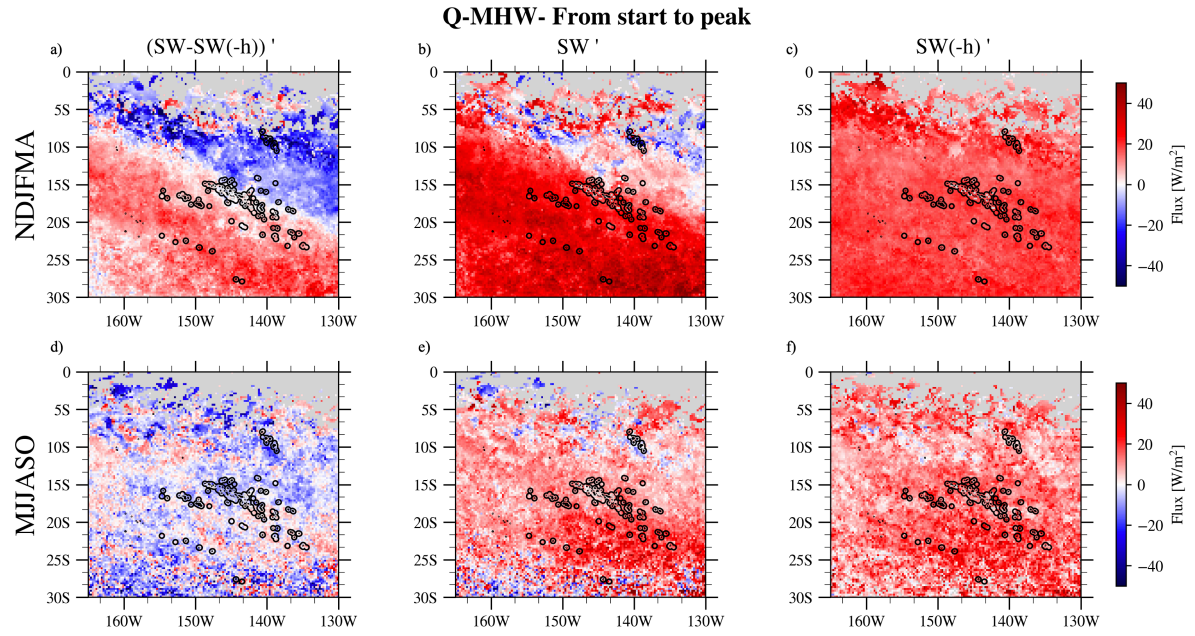

Figure S13. Start to peak composites for Q-MHWs in austral summer (a-c) and austral winter (d-f) of the net short-wave flux term (a,d), the incident short-wave (b,e) and the downward leak of short-wave at the bottom of the mixed layer (c,f).

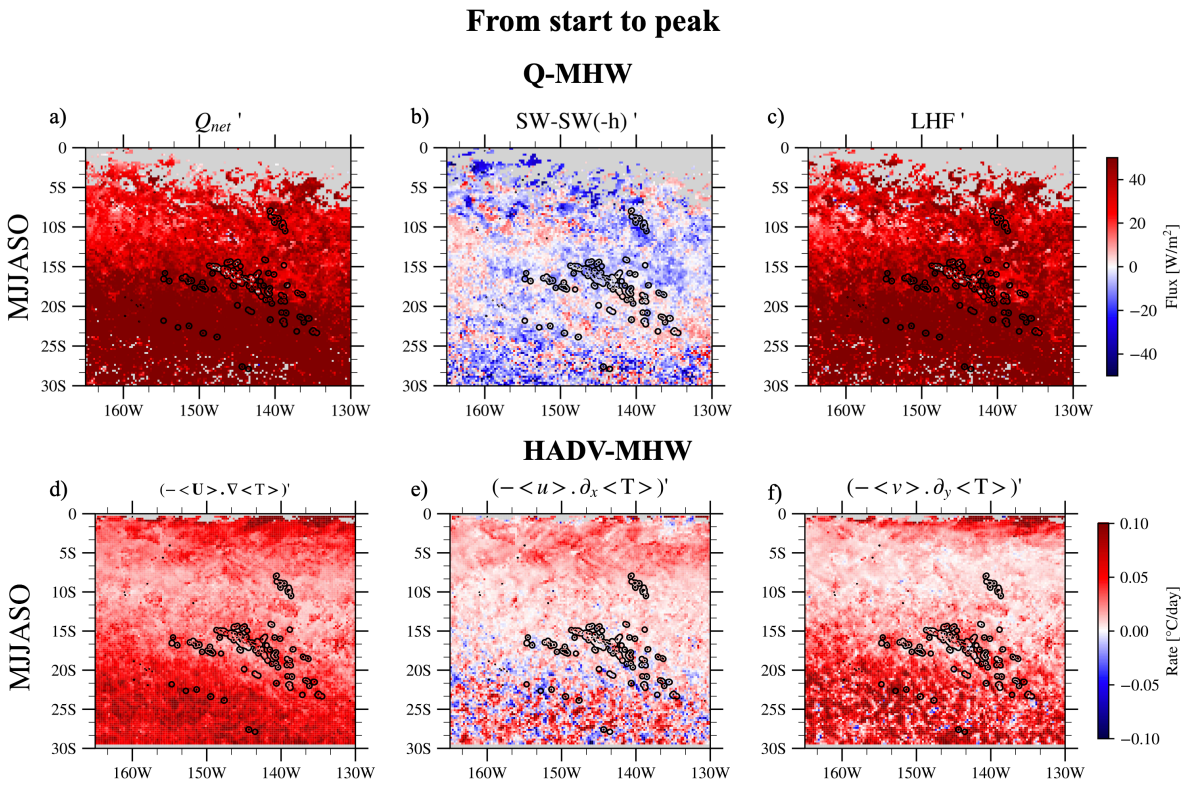

Figure S14. Same as Fig. 7 but for austral winter.

Role of Q' and h' in the variation of $\left(\frac{Q_{net}}{\rho c_p h}\right)'$

The respective roles of the air/sea flux and the MLD variations (h') in explaining the mixed layer temperature variations during the onset and decay of MHWs were investigated as follows. As Q is a function of the MLD (via the SW(-h) term, see Eq. 4), we considered here the term Q* standing for Qnet without subtracting the part of short-wave incident flux that escapes downward under the mixed layer. In order to disentangle which of Q*' and h' plays the most important role in the rate of temperature change of radiative term described in the figure above, we decomposed it following the method of Morioka et al., (2012) :

$$\left(\frac{Q^*}{\rho c_p h}\right)' = \frac{Q^{*\prime}}{\rho c_p \overline{h}} - \frac{h'\overline{Q^*}}{\rho c_p \overline{h^2}} + NL(Q^{*\prime}h') \quad \text{(S1)}$$

where the non-linear term NL(Q*′h′) includes second-order interactions between anomalies of surface heat flux (Q*') and mixed layer depth (h′). Here, overbars denote seasonal climatologies, and primes (′) represent interannual anomalies (i.e., the seasonal cycle has been removed). $\frac{Q^{*\prime}}{\rho c_p \overline{h}}$ corresponds to the role of variations in air/sea fluxes and $\frac{h'\overline{Q^*}}{\rho c_p \overline{h^2}}$ the role of variations in mixed layer thickness in explaining the overall variations of $\left(\frac{Q*}{\rho c_p h}\right)'$.

Fig. S15 enables us to quantify the contribution from the air/sea flux and the mixed layer variations to the total effect of the net heat flux budget term in austral summer and winter during Q-MHWs' onset.

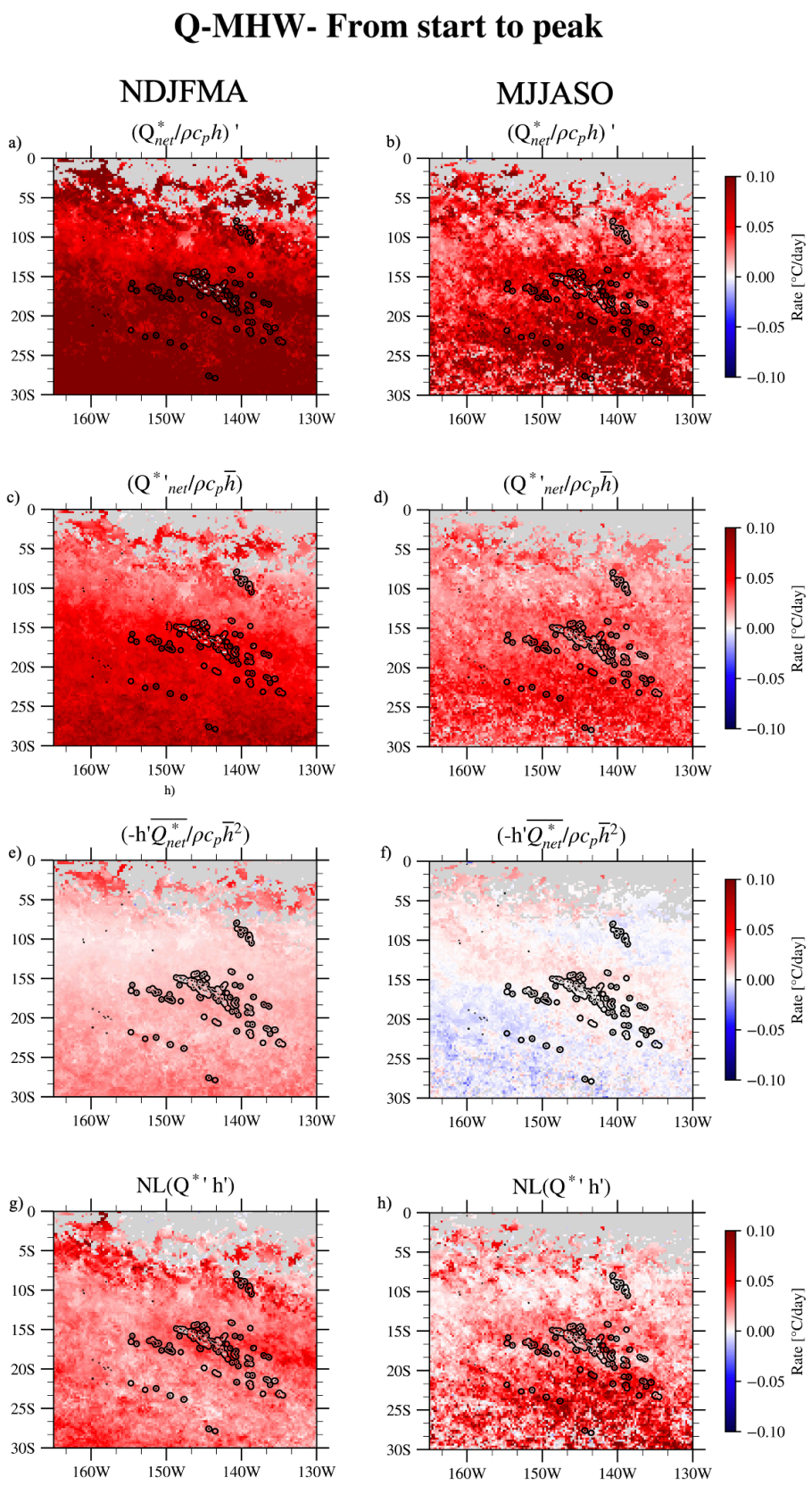

Figure S15. Average for Q-MHWs from start time to peak time for austral summer (a,c,e,g) and austral winter (b,d,f,h) of the total net air-sea flux term anomalies $(Q*/\rho c_p\, h)'$ (a and b) and its decomposition in terms of Q*' (c,d) and h'(e, f) contributions and as well as the non-linear term NL(Q*'h') (g, h), see Eq. (S1) for the equation of the decomposition.

Reynolds decomposition of horizontal advection

To better understand the horizontal advection anomalies observed during MHW onset and decay, we further decomposed this term using Reynolds decomposition ($u=\bar{u}+u'$, $v=\bar{v}+v'$, $T=\bar{T}+T'$, where overbars stand for climatology computed over the whole period and ' for anomalies with respect to it). To specifically isolate the role of current and temperature gradient variations from mixed layer variations, we analyzed the horizontal currents averaged over a fixed depth of 0–30 m here ($< U >_{30}$. $\nabla < T >_{30}$). For readability concerns $< U >_{30}$ and $< T >_{30}$ are written **U** and T here.

The horizontal advection was decomposed as:

$$-(\boldsymbol{U} \,.\, \nabla T)' = -(\bar{\boldsymbol{U}}.\nabla T' + U'\nabla\bar{T} + U'\nabla T' - \overline{U'\nabla T'}) \quad \text{(S2)}$$

$$-(\boldsymbol{U} \,.\, \nabla T)' = -(\bar{u}\partial xT' + \bar{v}\partial yT' + u'\partial x\bar{T} + v'\partial y\bar{T} + u'\partial xT' + v'\partial yT') + \overline{u'\partial xT' + v'\partial yT'} \quad \text{(S3)}$$

The term $\overline{u'\partial xT' + v'\partial yT'}$ has been computed and found to be negligible. The different terms of this decomposition are presented in Fig. S16 averaged from start to peak over all HADV-MHWs for all months.

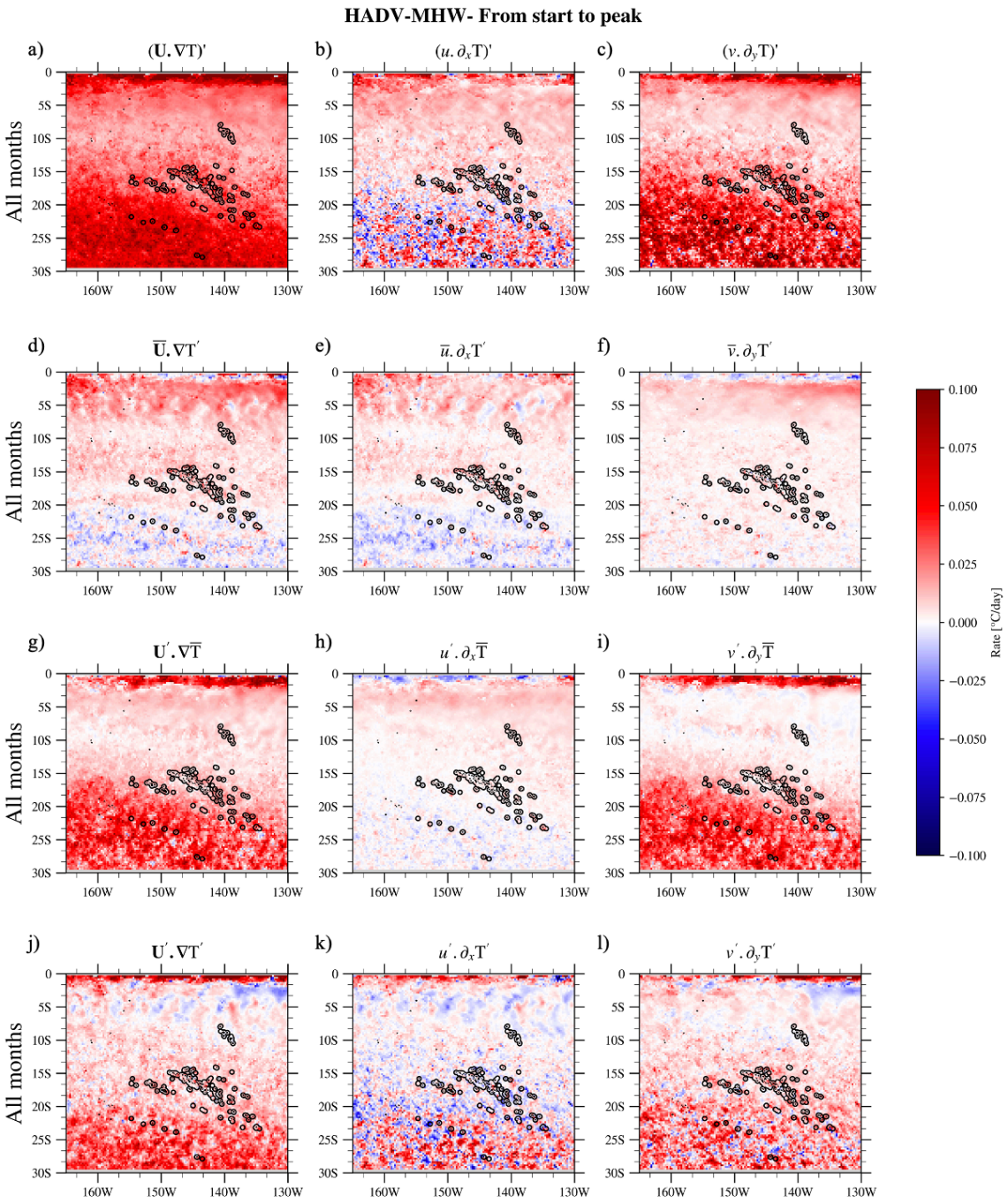

Figure S16. Start to peak HADV-MHW composites of horizontal advection term (with temperature and currents average from the surface to 30m) and its zonal and meridional Reynolds decompositions (u=ū+u′, v=v̄+v', T=T̄+T'). Panels a,d,g,j represent the composite of the different terms of Eq. (S2). Panels b, e, h, k show the zonal terms of Eq. (S3), and panels c, f, i, l show the meridional terms of Eq. (S3). Both seasons were taken into account to compute the composite as no real differences between both appeared here.

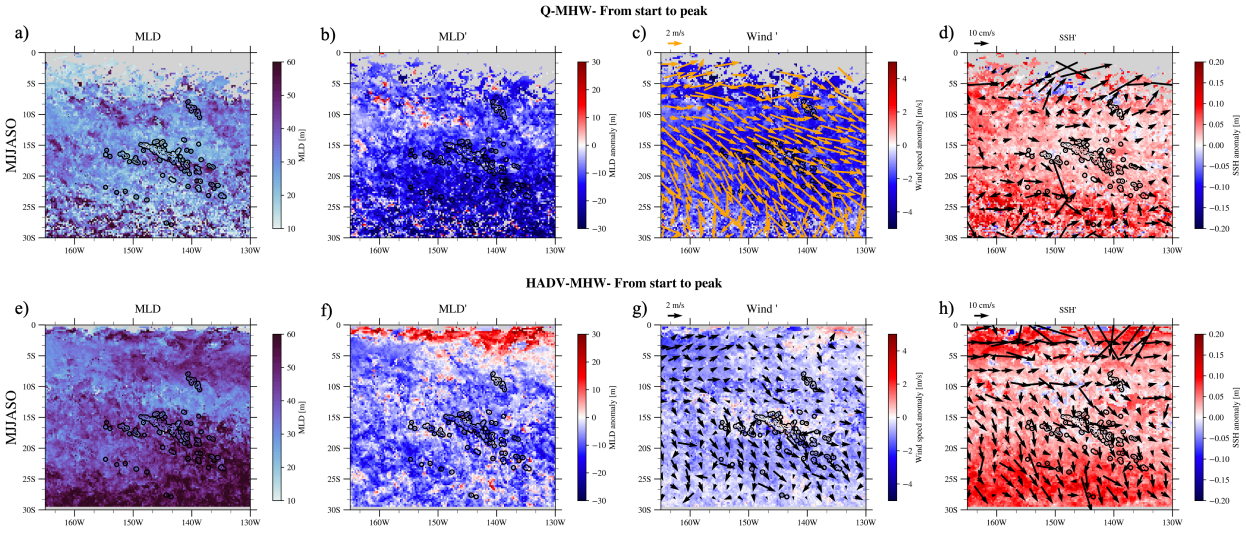

Figure S17. Same as Fig. 8 but for cold season.

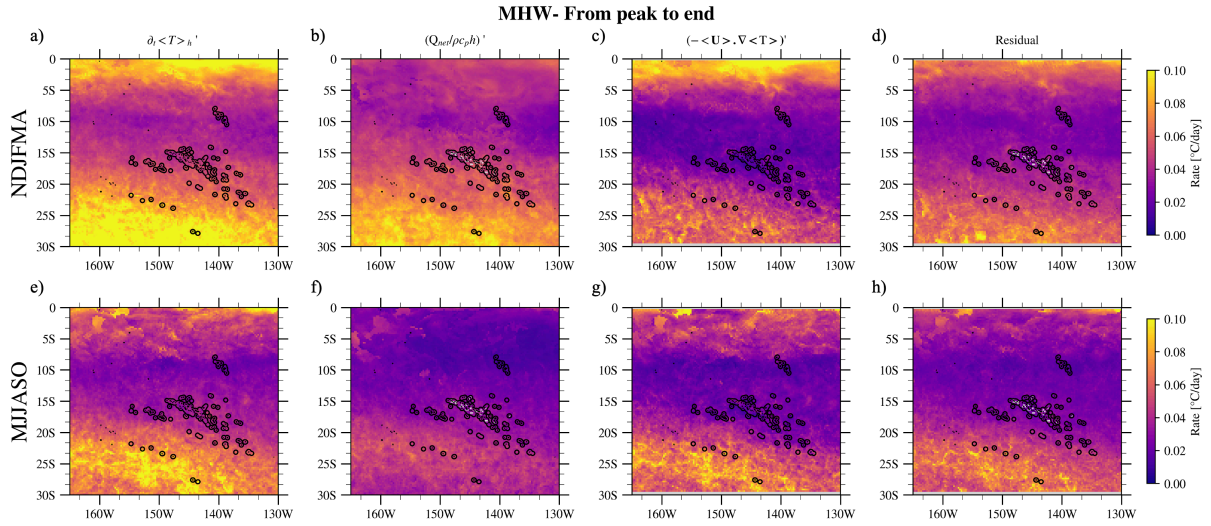

Figure S18. Standard deviation associated to the mean composites of the heat budget terms of Eq. (2) presented in Fig. A2.

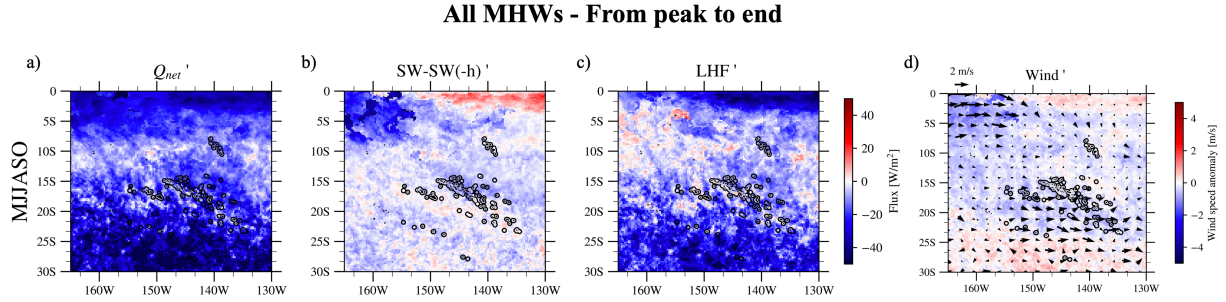

Figure S19. Same as Fig. 9 but for austral winter.

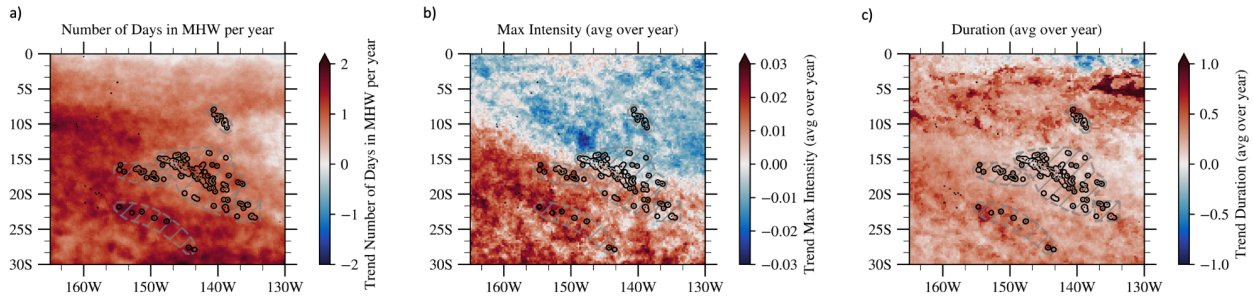

Figure S20. Linear trend of the number of days in MHW, the max intensity and the duration over the 1981-2024 period in OISST. The trend is expressed in number of MHW days per year (a,c), °C per year (b).